Generation of midfield concentrated beam arrays using periodic metal annular apertures

Hwi Kim,[1] Jaebum Cho,[2] Jihwan Park,[1] Seungoh Han,[3] and Sungkyu Seo[1,*]

[1]Department of Electronics and Information Engineering, Korea University, Jochiwon 339-700, South Korea

[2]School of Electrical Engineering, Korea University, Seoul 136-713, South Korea

[3]Research Center for Convergence Technology, Hoseo University, Asan 336-795, South Korea

*Corresponding author: sseo@korea.ac.kr

Received 26 August 2011; revised 17 November 2011; accepted 17 November 2011; posted 18 November 2011 (Doc. ID 153469); published 6 March 2012

Generation of minimally diffracting beam arrays in the midfield region using periodic metal annular apertures is investigated. The relations between the patterns of the diffraction fields and the structural parameters of the periodic metal annular aperture are numerically analyzed. Material dependent transmission characteristics are also studied with finite difference time-domain simulation. The results reveal that the beam concentration efficiency and axial intensity uniformity have a trade-off restriction due to strong inter-aperture interference and surface plasmon mediates the transmission efficiency of the periodic annular apertures. The design criteria of the metal annular aperture to achieve the strong and uniform beam arrays are addressed. © 2012 Optical Society of America

OCIS codes: 050.1970, 240.6680, 170.2945.

1. Introduction

Long working distance (WD) and depth-of-field (DOF) of a focusing device in a diffraction limited system are critical factors to be considered for various applications including biological sensing and lithography. The former often needs to image the interiors of cells rather than the surfaces, and the latter usually needs to expose a resist layer of a certain thickness. The WD and DOF of a focusing device are mainly restrained by the issues associated with divergent diffraction and low-transmission efficiency. To address these issues, recently, subwavelength metallic structures including metallic holes [1,2], slits [3–5], surface corrugations [6], or gratings [7,8] have been heavily studied. These subwavelength structures, usually periodic metal nano structures, can efficiently excite surface plasmon (SP) waves and also generate directional beaming effects by radiating SP waves to propagating optical fields. Although these are not in the form of conventional optical lenses, they work as planar objective lenses whose optical waves can propagate up to several wavelengths from the metal surface [9] or be strongly bound to the metal/dielectric interface as SP enhanced focal spots [10]. Performing a focusing function without any traditional optical lenses, this type of planar objective lenses may be useful for enabling a compact, lightweight, and field-portable microscope [11] or super resolution imaging [12]. While the periodic nanostructured arrays of such a planar or beaming device can remarkably enhance the light throughput, they also degrade the beam quality severely due to the strong interference between adjacent elements in the periodic arrays.

In this paper, the optimal conditions to synthesize the high-quality beam arrays utilizing periodic metal annular apertures are investigated numerically [Fig. 1(a)]. In particular, for some biological sensing and lithography applications, it is needed for the WD of a planar objective lens to be placed in the range from 1 μm to 10 μm within the visible light wavelength band. This WD range is specifically referred

1559-128X/12/081076-10$15.00/0
© 2012 Optical Society of America

to as the "midfield region" in this paper. From the physical viewpoint, the midfield region for an annular aperture is defined by an overlapped nonparaxial region. The free space can be divided into paraxial and nonparaxial regions in the viewpoint of the wave optic theory. For the annular aperture structure, the nonparaxial optical fields diffracted by the aperture are overlapping in the central finite region due to the circular symmetry. The overlapped nonparaxial region, i.e., the midfield region illustrated in Fig. 1(b), is distinguished from the paraxial or nonparaxial region, since a tightly concentrated finite beam can be formed in that region. Within the visible light band, the position of the midfield region can be placed to a specific region of interest, i.e., in the range of 1 μm to 10 μm for biological sensing and lithography, by tuning the width and radius of the annular aperture. In Fig. 1(a), the annular aperture array is parameterized by the structural parameters of outer radius (R), width (W), and period (P), and the resulting diffraction beams are illustrated.

The main target of this study is to create high-quality diffraction beam arrays within a minimal device area; thus the period of the array is supposed to be several times of the operating wavelength. The axial focusing efficiency and distributive intensity uniformity are important quality factors of the diffractive beam array. To achieve this goal, the numerical analysis is unfolded in two steps. First, in Section 2, design rules of periodic metal annular apertures are studied based on the scalar wave optic model. Almost all possible combinations of structural parameters are examined with efficient and relevant wave optic simulations to find the optimal structural condition for small and strong beaming with axial uniformity in the midfield region. Second, in Section 3, material for the periodic annular apertures is considered as another critical factor. Since the material consideration can be explained by Maxwell's equations, the optical transmission efficiency of the periodic metal annular apertures is studied with the finite difference time domain (FDTD) method. The result shows that the suitable material selection for enhancing the optical transmission efficiency has a close relationship to the SP excitation. Section 4 summarizes the performance of the periodic metal annular aperture and its possible applications in various fields.

2. Optimal Design Rule of Periodic Metal Annular Apertures

In this section, the annular aperture diffraction is described by the scalar wave optic model. Assuming that the annular aperture of Fig. 1(a) is illuminated by a normally incident circularly polarized plane wave from the fused silica side, then the annular aperture diffracts the incident light and forms a concentrated beam profile in the midfield region. Since the beaming effect of the annular aperture is observed in the nonparaxial region, it is necessary to employ the angular spectrum representation for the accurate description of the nonparaxial diffraction field distribution. And this angular spectrum representation takes the form of

$$F(x,y,z) = \int_{-\infty}^{\infty}\int_{-\infty}^{\infty} A(\alpha,\beta)\exp(j2\pi(\alpha x + \beta y + \gamma z))\mathrm{d}\alpha\mathrm{d}\beta, \tag{1a}$$

where α and β are x- and y-directional spatial frequency components. The z-directional spatial frequency, γ, is $\sqrt{(1/\lambda)^2-\alpha^2-\beta^2}$, and $A(\alpha,\beta)$ is the two-dimensional Fourier transform of an annular aperture with outer radius of R and inner radius of r given by

$$A(\alpha,\beta) = \begin{cases} \frac{RJ_1(2\pi R\sqrt{\alpha^2+\beta^2})}{\sqrt{\alpha^2+\beta^2}} - \frac{rJ_1(2\pi r\sqrt{\alpha^2+\beta^2})}{\sqrt{\alpha^2+\beta^2}} & \text{for } (\alpha,\beta)\neq(0,0) \\ \pi R^2 - \pi r^2 & \text{for } (\alpha,\beta)=(0,0) \end{cases}, \tag{1b}$$

where $J_1(R)$ or $J_1(r)$ is the Bessel function of the first kind, order 1. Then, the light field generated by the annular aperture array with x- and y-directional

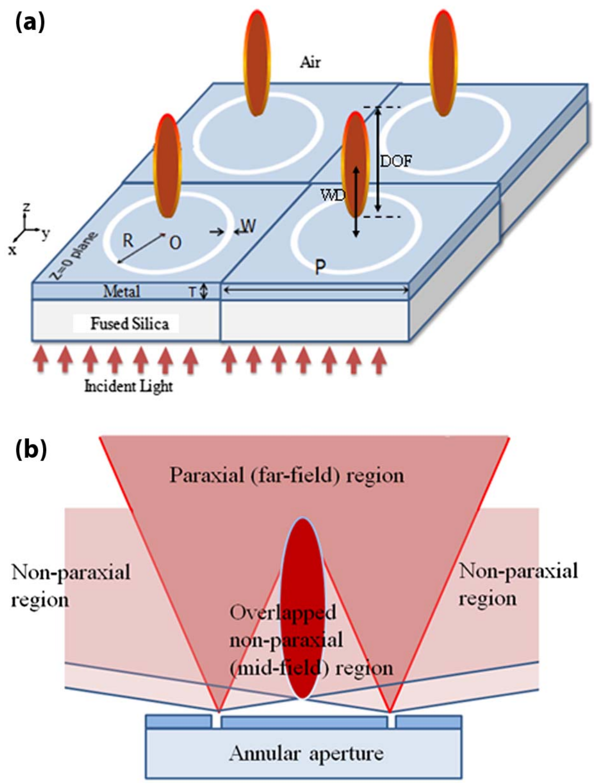

Fig. 1. (Color online) (a) Structure of periodic metal annular apertures. Annular apertures are structured in a highly conductive metal layer on a fused silica substrate. R, r, W, T, and P denote aperture outer radius, aperture inner radius, aperture width, metal thickness, and period, respectively. The interface between metal and air is defined as $z = 0$ plane and the optical axis is z-axis. (b) Midfield region defined by the overlapped nonparaxial region.

periods of P is represented by

$$F_P(x,y,z) = \sum_{k=-\infty}^{\infty} \sum_{l=-\infty}^{\infty} F(x - kP, y - lP, z), \qquad (2)$$

where k and l are the running indices of the double summation operator. The above formulation is scalable and invariable for wavelength. Thus, if the wavelength changes, diffraction field profile is obtained by scaling spatial variables with the wavelength. Even though we use the spatial variables normalized by wavelength, $(x/\lambda, y/\lambda, z/\lambda)$, the relative field profiles do not change. In the following simulations, diffraction field profiles are presented for the normalized spatial variables.

Figure 2 illustrates exemplary simulations of light fields diffracted by periodic annular apertures with a few different normalized aperture periods. The normalized aperture outer radius R/λ and width W/λ are set to 1.9318 (850 nm/440 nm) and 0.7955 (100 nm/440 nm), respectively. These normalized radius and width values are used for all cases illustrated in Fig. 2, where the normalized periods of the aperture array in Figs. 2(a–d), P/λ, are 18, 10, 6, and 3, respectively. The simulation result in Fig. 2(a) shows that the annular aperture makes a fine locally concentrated beam with long working distance in the midfield region effectively, while those in Figs. 2(b–d) demonstrate that the inter-aperture interference degrades the light field profiles significantly. As seen in Figs. 2(b–d), the coherent fluctuation in the axial intensity profile restricts the axial uniformity of the local beam in a finite midfield region. In this paper, the short and long midfield regions are defined with the reference position of $z/\lambda = 4$ indicated by a white dashed line in each of Fig. 2, i.e., the upper and lower part of the dashed line are long and short midfields, respectively.

We define two measures to evaluate the diffraction field profiles quantitatively: (i) axial intensity density $\frac{1}{z_2 - z_1} \int_{z_1}^{z_2} |F(0,0,z)| \mathrm{d}z$ and (ii) axial intensity variance, $\underset{z_1 \le z \le z_2}{\mathrm{var}} (|F(0,0,z)|)$, which represent the statistical average and variance for the axial intensity profile in the range of $z_1 \le z \le z_2$, respectively. The axial intensity density signifies the beam concentration efficiency, while the axial intensity variance addresses the uniformity of the axial intensity profile.

In this work, light field distributions of 59,640 samples, prepared by the combinations of structural parameters with 50 nm increments in both outer radius (from 550 nm to 4000 nm) and width (from 50 nm to 3500 nm), and 100 nm increment in period (from 1100 nm to 8000 nm) for the reference wavelength of 440 nm, are examined. For a specific axial region, $z_1 \le z \le z_2$, the axial intensity variances of the obtained field distributions are computed with the variation in the period. The samples that have the axial intensity variance of less than 10% are selected for further consideration. This is the first qualifying threshold in the design of the beam array. The maximum, minimum, and average values of both the axial intensity density and the axial intensity variance are extracted for the samples selected.

In our simulation, the bottom position of the midfield region is fixed to 1.1364, which corresponds to 500 nm for the reference wavelength of 440 nm. For some biological sensing applications, e.g., lensfree imaging of blood cells whose sizes ($d = 1$–10 μm) vary with cell species [13], it is critical that the specimen should be placed close to the sensing substrate, i.e., the periodic annular aperture arrays, within the midfield region where the concentrated beam arrays can illuminate the cells with a uniform and strong beam profile. Furthermore, for lithography application, the thickness of some widely utilized photoresist layer, e.g., AZ5214E or SU-8, ranges from 1–100 μm depending on the model and spinning speed. For reference, numerous periodic metal annular aperture arrays integrated within a chip may work as a high-throughput direct writing device for maskless nanolithography [9]. While the lower limit of the midfield region is limited by the specific applications, the upper limit of the midfield region of interest can be flexibly determined with respect to other practical applications. In

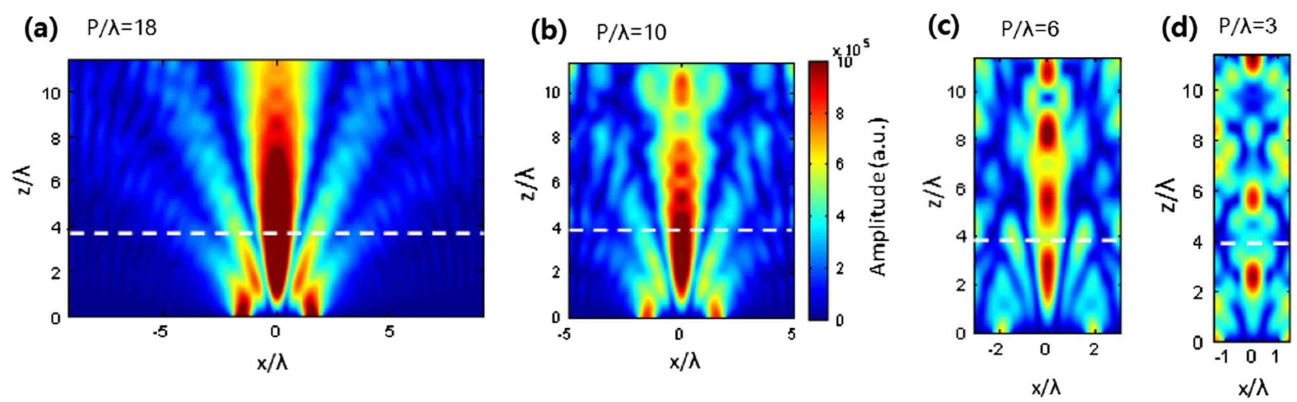

Fig. 2. (Color online) Optical field profiles generated by metal periodic annular apertures with the periods (a) $P/\lambda = 18$, (b) $P/\lambda = 10$, (c) $P/\lambda = 6$, and (d) $P/\lambda = 3$. The reference length of the midfield region ($z/\lambda = 4$) is indicated by a white dashed line. The reference wavelength is 440 nm.

Fig. 3(a), the maximum, minimum, and average values of the axial intensity density and the axial intensity variance versus period are graphed in the left and right sides, respectively, for a specific axial region. In this case, the region of interest is set to a midfield region of $1.1364 < z/\lambda < 2.2727$ in the unit of the wavelength normalized spatial variables.

The simulations are performed for the reference wavelength of 440 nm without loss of generality caused from the scalability in Eq. (1a). For this wavelength, the bottom starting point of the midfield region is supposed to be in the position 500 nm over the metal surface. The ratio of the starting position and the reference wavelength, 500 nm/440 nm, is 1.1364. Considering the scalability, we use this dimensionless value 1.1364 as the bottom position of the midfield region for all simulations in this paper. For the reference wavelength, the lengths of 1 μm, 2 μm, 3 μm, and 4 μm are used for the simulation study, which are equal to dimensionless values 2.2727, 4.5455, 6.8182, and 9.0909, respectively.

As the period, i.e., the interdistance between adjacent annular apertures, gets shorter, the axial intensity variance tends to degrade, while the beam concentration efficiency increases. We can also observe some variations of the graphs by incrementing the region of interest. In Figs. 3(b–d), the axial intensity density and axial intensity variance versus period are presented for the selected midfield region of $1.1364 < z/\lambda < 4.5455$ and the axial ranges extended to the midfield regions of $1.1364 < z/\lambda < 6.8182$, and $1.1364 < z/\lambda < 9.0909$, respectively. As the period increases, both the axial intensity density and the axial intensity variance decrease simultaneously.

A large period leads to the small fill factor of the opening area in the aperture arrays, and the small fill factor results in a decreased intensity density. For the axial intensity variance, however, the larger period also minimizes the inter-aperture interference between adjacent annular aperture arrays. This reveals that there is a trade-off between beam concentration efficiency and beam profile uniformity in the midfield regions. This trade-off relationship of the light field profiles can be understood more effectively by Fig. 4. In Fig. 4, the maximum values of the axial intensity density (beam concentration efficiency) and axial intensity variance (beam profile uniformity) are visualized for the length of the midfield region and the period.

In Figs. 2(c,d) (the samples with periods of $P/\lambda = 6$ and $P/\lambda = 3$), a single lobe is well defined within the specified midfield region of $z/\lambda \leq 4$. The inter-aperture interference makes the length of the midfield region shorten as the period decreases. As mentioned before, in this analysis, we extracted the specific samples that have an axial intensity variance of less than 10% among the 59,640 calculated sample pools. The selected samples can be changed by the definition of the axial region of interest. The samples used in Figs. 3(a,b) are selected for the short midfield region under the reference length of $z/\lambda = 4$, while those of Figs. 3(c,d) are chosen for the long midfield region over the reference length of $z/\lambda = 4$.

Comparing the axial intensity density of those two groups, we can find some interesting features in both the short and long midfield regions. The axial intensity density presented in Figs. 3(c,d) for the region of $P/\lambda > 15$ is much flatter and more stable than that of the region of $P/\lambda < 15$. Large fluctuation of the axial intensity density, for the midfield region with a length smaller than $z/\lambda = 4$, may be the result of massive inter-aperture interferences, while the flat axial intensity density for the midfield region greater than $z/\lambda = 4$ can be translated as the effective optical separation of the apertures. Thus the condition of $P/\lambda > 15$ can provide the minimal intensity variance, and so designing the periodic annular apertures within the region of $P/\lambda > 15$ is recommended for the strong and uniform beam arrays in the long midfield region. On the other hand, it is noteworthy that the graphs of the axial intensity variations in Figs. 3(a) and 3(b) show a dip around the period of $P/\lambda = 4$, while those in Figs. 3(c) and 3(d) reveal monotonically decreasing feature in the axial intensity variation. The axial intensity integration has a consistent feature of linear decrease with the period without respect to the length of the midfield region. This feature observed in the low axial intensity variation region around the dip provides another clue for finding optimal periodic annular apertures for the short midfield region.

3. Material Dependent Transmission Efficiency of Periodic Metal Annular Apertures

To investigate the influence of material on the transmission efficiency for the annular aperture structure, several highly conductive metals, such as Al, Au, Ti, and Ag, which also have been widely studied by many plasmonics research groups [1,2,5,8–10,12,14], are tested with an exemplary design of the annular aperture, i.e., R1025W350P8000 implying 1,025 nm aperture outer radius (R), 350 nm aperture width (W), and 8,000 nm period (P). To set the single aperture design as R1025W350P8000, considerable amounts of scalar field calculations, i.e., 59,640 samples, were performed with various aperture radii, aperture widths, and periods, as discussed in Section 2. The period of the metal annular apertures was set to 8 μm, which corresponds to the normalized periods around $P/\lambda > 15$, where the axial intensity density and the intensity variation minimally fluctuate, as shown in Fig. 3. We have also varied metal thickness from 50 nm to 200 nm. However, in this section, we fix the thickness to 100 nm to investigate the material effect more objectively.

For the numerical analysis, we use time-domain electromagnetic massively parallel evaluation of scattering from topography, a Maxwell equations solver based on the three-dimensional FDTD method. Circularly polarized monochromatic light of $\lambda = 300 \sim 580$ nm is assumed to be incident on the fused silica side of the annular aperture device. The simulation node size is specified as 20 nm, i.e., less than

$\lambda/15$, for all the numerical calculations in this section. The perfectly matched layer, a nonphysical anisotropic material that absorbs incident radiation from various angles without reflection, is employed at the top and bottom boundary regions of the simulation domain, and the periodic boundary condition

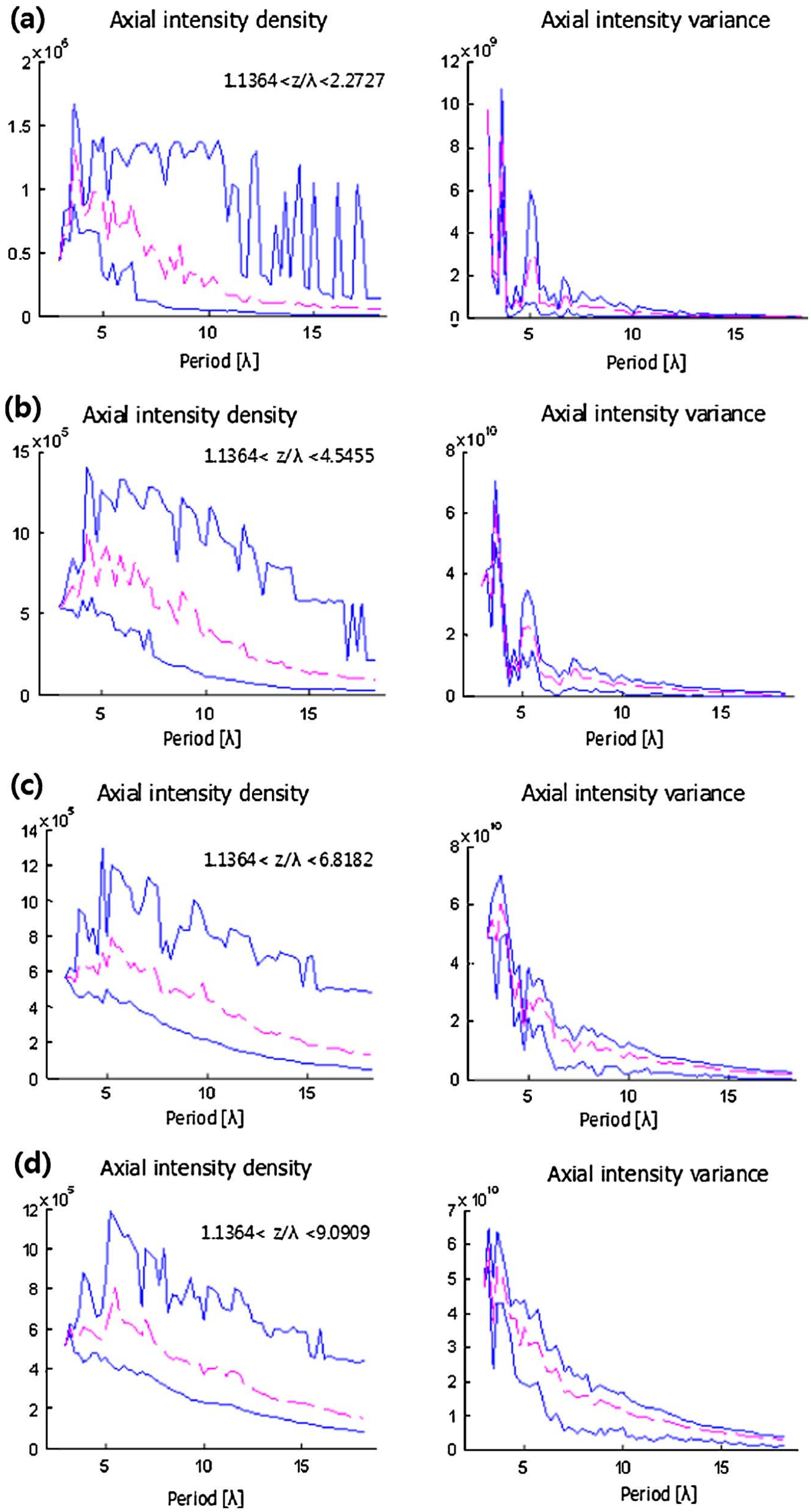

Fig. 3. (Color online) Axial intensity density and axial intensity variance for the midfield ranges: (a) $1.1364 < z/\lambda < 2.2727$, (b) $1.1364 < z/\lambda < 4.5455$, (c) $1.1364 < z/\lambda < 6.8182$, (d) $1.1364 < z/\lambda < 9.0909$. The reference wavelength is 440 nm.

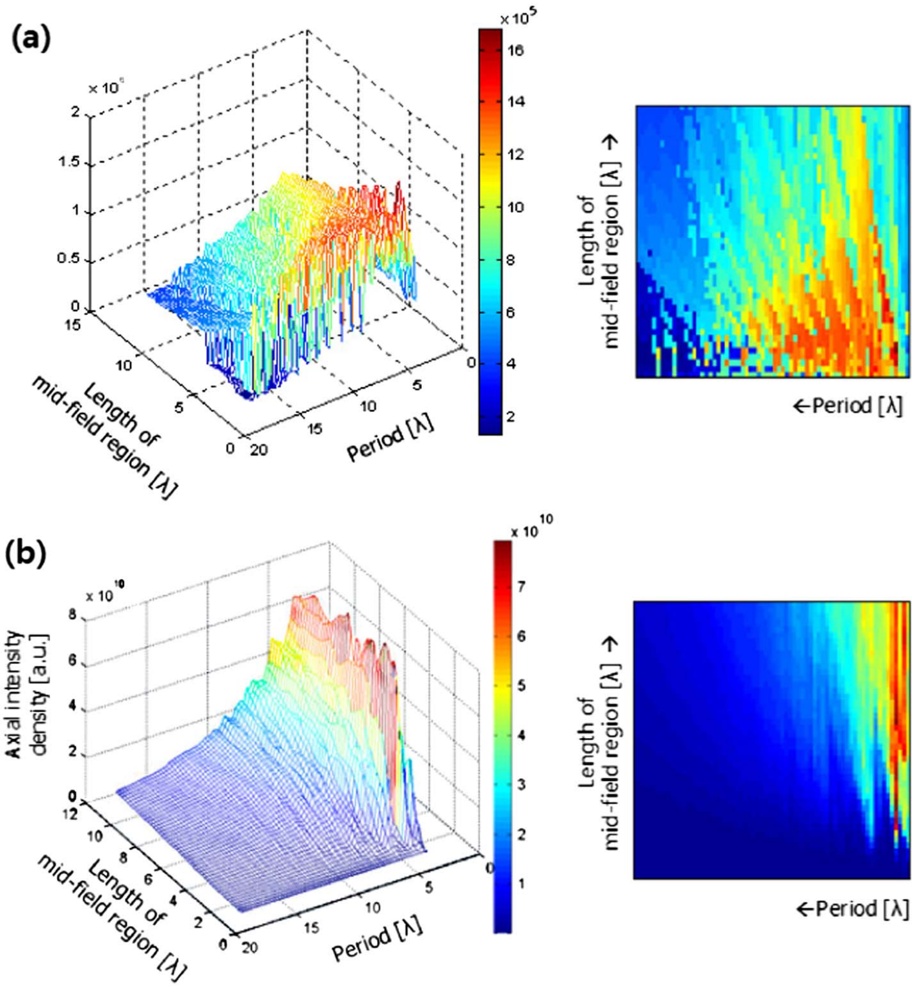

Fig. 4. (Color online) Graphical representations of (a) the maximum values of the axial intensity density and (b) the maximum values of axial intensity variance evaluated for the samples included in the lower 10% among 59,640 calculated sample pools. The reference wavelength is 440 nm.

is applied to the four sides enclosing the simulation space to represent the periodic structure.

Figure 5 shows the light transmission characteristics of an Ag annular aperture within the exemplary design. Since most of the highly conductive metals are dispersive materials, the Ag annular aperture also shows the frequency dependent transmission, as shown in Fig. 5(a). Note that light transmission through the Ag annular aperture has a resonant illumination wavelength point at $\lambda = 360$ nm, regardless of the axial point, e.g., $z = 1{\sim}5$ μm [Fig. 5(b)]. The concentrated beam generated by the Ag annular aperture propagates more than 5.4 μm from the metal surface.

The transmitted light intensity for the annular apertures structured in various metals, i.e., Al, Au, Ti, and Ag, was compared in Fig. 6 to elucidate the material effect and fix the material of interest. Metal annular apertures are uniformly illuminated by 360 nm circularly polarized plane waves, sharing the exemplary design parameter of R1025W350 P8000. Figure 6(a) compares, graphically, the transmitted light intensity in the x-z and x-y planes for the various metals, i.e., Al, Au, Ti, and Ag, with the same aperture design. As illustrated in Fig. 6(b), light intensity passing through the Ag annular aperture is much higher than that of other metals and it has a maximum transmission at $z = 1.58$ μm. Same metal slabs were also simulated without employing the annular aperture structure, i.e., bare thin metal films, to evaluate the direct transmission property of the thin metal films investigated. According to the FDTD simulation results of Fig. 6(c), a 100 nm thick Ag slab, i.e., without aperture, also transmits more incident light than other metals; however, this is less than 2% compared to the peak transmitted light intensity through the Ag annular aperture shown in Fig. 6(b).

The physical background of the transmission differences for various materials may be attributed to the excitation of surface plasmon. For the strong induction of SP waves, material consideration, i.e., metal-dielectric combination, has been one of the critical factors as explored by many research groups [1,2,4,12]. In this work, we employ air for the dielectric medium in the region of $z > 0$. Broadband SP

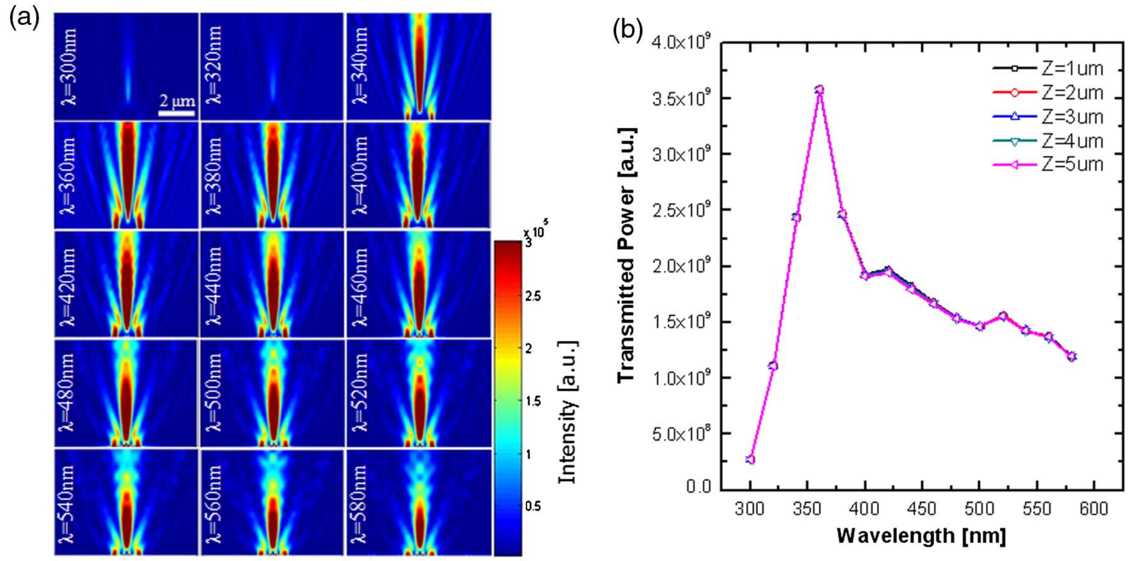

Fig. 5. (Color online) Wavelength dependent light transmission characteristics of metal annular aperture. (a) Light intensity variation of the Ag annular aperture under the illumination wavelengths of 300 ~ 580 nm. (b) Wavelength resonant property of the Ag annular aperture. Annular aperture design parameter used in these simulations is R1025W350P8000.

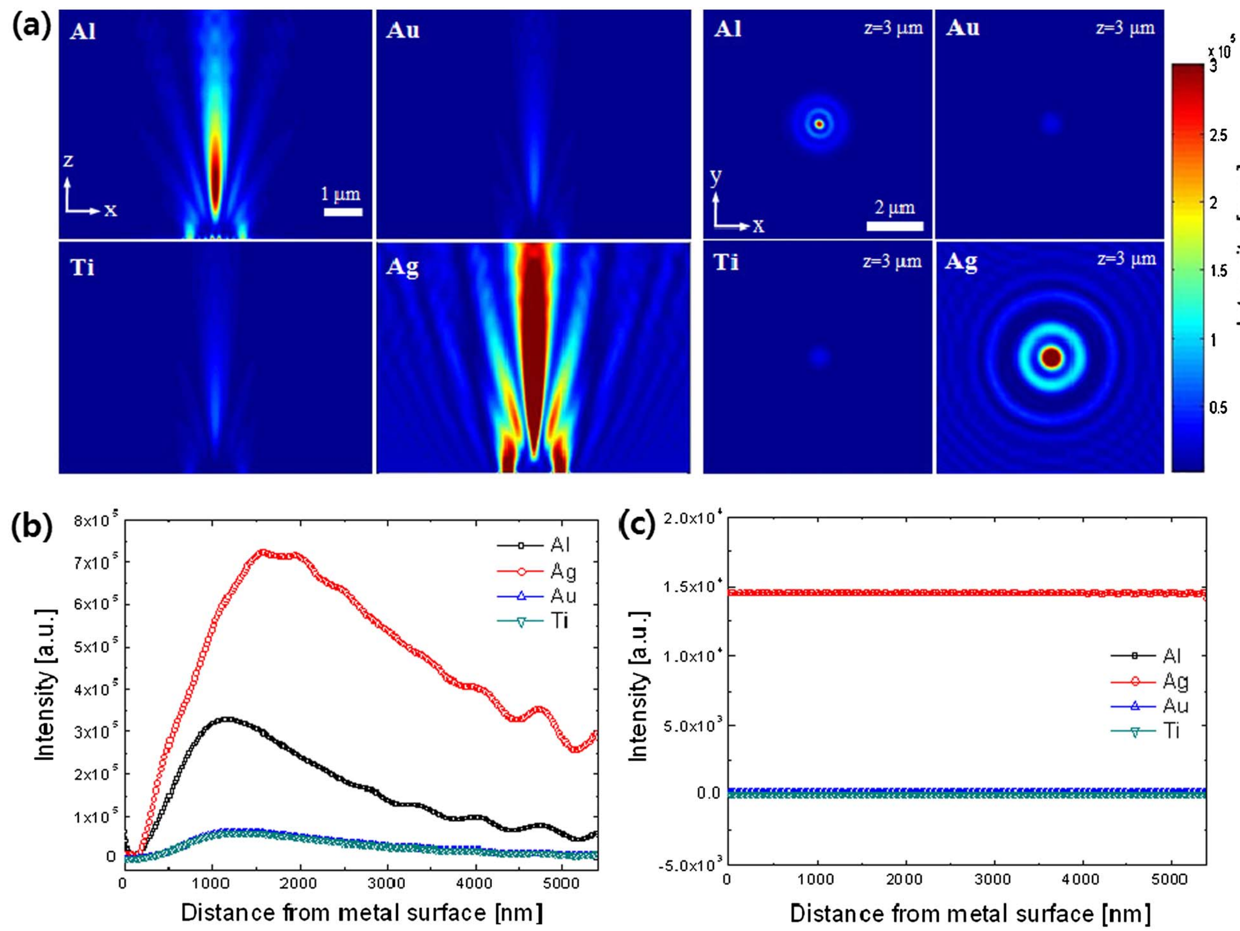

Fig. 6. (Color online) Light transmission properties of annular apertures structured in various metals. Annular apertures of various metals uniformly illuminated by 360 nm circularly polarized planewaves, within the design parameter of R1025W350P8000. (a) and (b) graphically compare the transmitted light intensity in x-z and x-y plane for the various annular apertures, i.e., Al, Au, Ti, and Ag. As illustrated in (c), light intensity passing through the Ag annular aperture is much higher than that of other metals and it has a maximum transmission at $z = 1.58$ μm. (d) Transmitted light intensity through 100 nm thick metal slabs without the annular aperture structures.

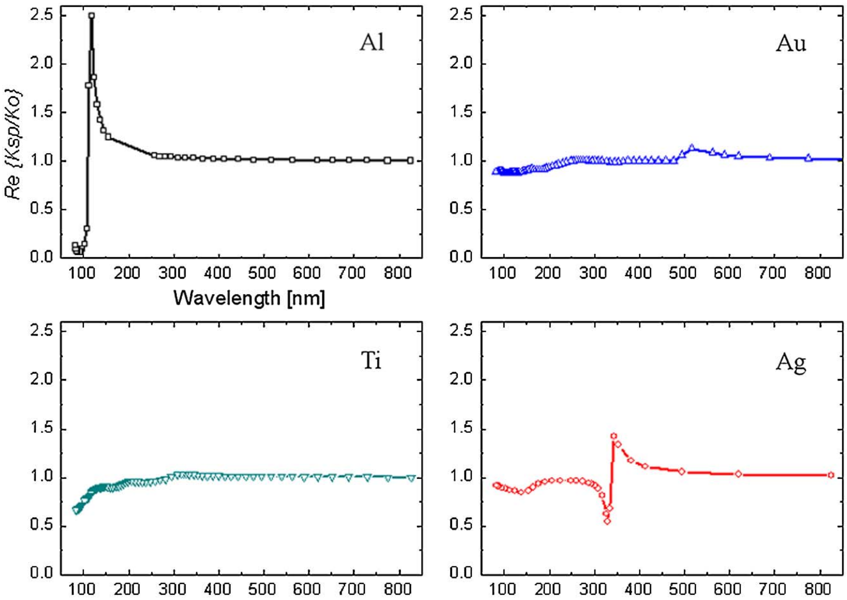

Fig. 7. (Color online) Broadband SP wavevector variation for the selected highly conductive metals interfacing air. Compared to other metals investigated, Ag shows relatively high SP wavevector, i.e., $\mathrm{Re}\{K_{\mathrm{sp}}/K_0\}$, in the wavelength ranges of 340 ~ 380 nm, which provided a clue in selection of the metal for strong SP excitation at the metal-air interface.

wavevector variation, for the selected highly conductive metals interfacing air, was calculated and plotted in Fig. 7. SP wavevector $\mathrm{Re}\{k_{\mathrm{sp}}\}$ would be simply derived from Maxwell's equation as $k_{\mathrm{SP}} = \frac{2\pi}{\lambda_0}\sqrt{\frac{\varepsilon_m}{\varepsilon_m+1}}$, where ε_m is the complex permittivity of the metal [2]. Frequency dependent complex permittivity values were collected from the complex refractive indices measured in the literature [15]. As shown in Fig. 7, Ag shows relatively high SP wavevector, i.e. $\mathrm{Re}\{k_{\mathrm{sp}}/k_0\} = 1.3 \sim 1.5$, in the wavelength ranges of 340 ~ 380 nm; this provided a clue in metal selection for high transmission efficiency. Note that the resonant point of the Ag annular aperture of

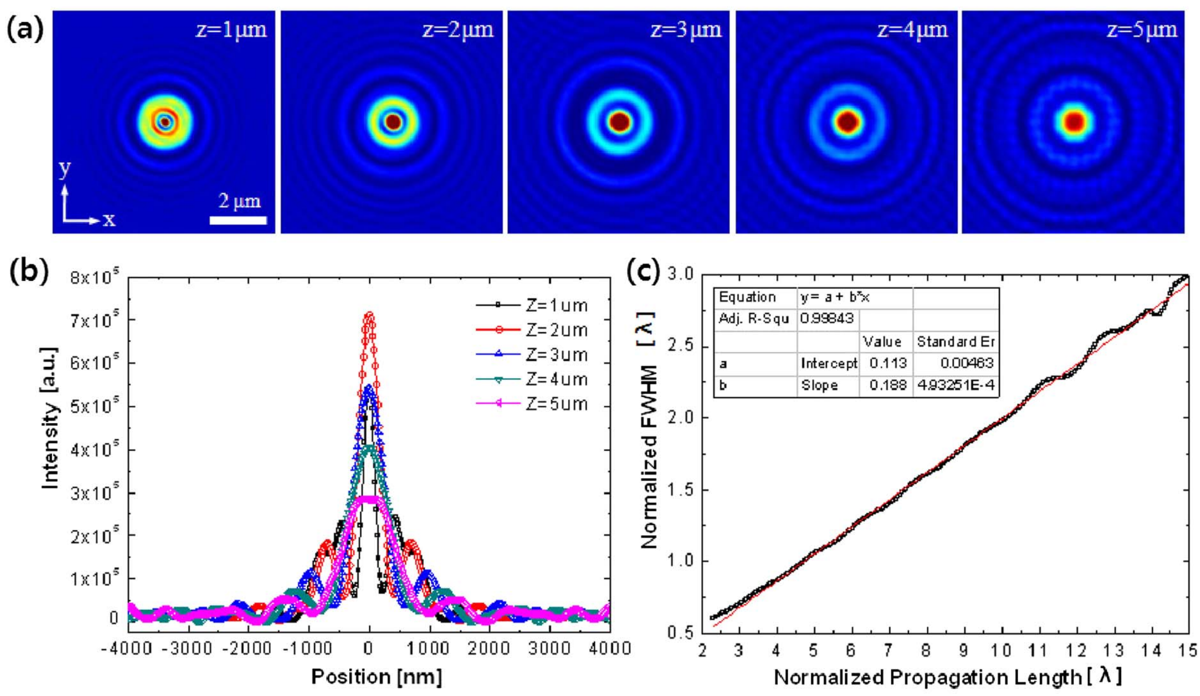

Fig. 8. (Color online) Beaming performance of the Ag annular aperture. (a) Focused light profile in x-y plane measured at $z = 1, 2, 3, 4,$ and $5\ \mu\mathrm{m}$. (b) The PSFs of the focused light measured in (a). (c) The FWHM values along with z-axis. The reference wavelength is 360 nm.

Fig. 5 matches well the wavevector calculations of Fig. 7, i.e. $\mathrm{Re}\{k_{sp}/k_0\}$.

Figure 8(a) graphs the light fields at different axial points of the Ag annular aperture to understand the beaming performance of the Ag annular aperture further. The incident light ($\lambda = 360$ nm) excites cylindrical SP waves from the edges of the apertures, and the interference of the SP waves with the zero-order transmitted wave creates a circular standing wave pattern, shown as the many concentric rings in the graph. This observation agrees with others' simulations and midfield measurements [2,14,16]. The point spread functions (PSFs) of the focused beam at different z-planes in Fig. 8(b) show that the transmitted light intensity after the maximum point, i.e., $z = 1.58$ μm, decreases with propagation distance gradually. However, at least 39% of the transmitted light measured at the maximum transmission point was delivered to the measurement point of $z = 5$ μm. The full-width-at-half-maximum (FWHM) values along the z-axis, i.e., $z = 2 \sim 15\lambda$, of the PSFs were also measured in Fig. 8(c). Note that the FWHM value at $z = 2\lambda$ was as small as 0.604λ, which is near the diffraction limit in optics. Also, the FWHM value was increased linearly, i.e., measured FWHM forms a linear graph with the adjusted coefficient of determination (R^2) of 0.99843, as a function of the distance from the Ag surface. This linear concentration property can provide a unique concentration function, especially in biological imaging and lithography applications.

Since the SP wave is cylindrical, the annular aperture actually acts similar to the apodization technique used to improve the resolution of far-field imaging systems. Toraldo di Francia suggested a method that uses a pupil of equally spaced concentric rings of alternating phase, so-called Toraldo filter, to make the first dark ring of the diffracted Airy pattern arbitrarily wide [17]. Other works also proposed various pupil filters to narrow the center lobe at the expense of energy leakage to side lobes [18–21]. Although the structure and material were optimized, the metal annular aperture of this study also accompanies the energy leakage from the side lobes. However, the annular aperture and apodization filter differ in three ways: (i) Apodization works in the Fraunhofer region, while the annular aperture works in the midfield region. (ii) Apodization works with lenses, while the annular aperture is a beaming element by itself. (iii) Apodization requires many annular apertures; however, the proposed device only employs a single annular aperture that can provide the structural and manufacturing simplicity.

4. Conclusions

According to the intensive scalar field calculations, it is found that there is a trade-off relationship between beam concentration efficiency and axial uniformity of the midfield beam arrays generated by periodic metal annular apertures. In particular, for the midfield definition of $z/\lambda > 4$, the region of $P/\lambda > 15$ provides a relaxed trade-off restriction, which promotes the generation of the concentrated beam arrays of strong, stable, and low intensity variance. A comparative study on material dependent transmission efficiency supports the role of surface plasmon for the significant transmission efficiency enhancement. A case study on the Ag annular aperture arrays within the optimized design parameter, i.e., R1025W350P8000, showed that the concentrated beam arrays as small as 0.604λ, approaching the diffraction limit in optics, can be generated and they propagate more than 15λ. The Ag annular aperture arrays, having many practical advantages, including ease of manufacture, small footprint, and structural simplicity, hold great promise in various applications, such as biological imaging, maskless nanolithography, and high-density data storage.

This research was supported by the Converging Research Center Program (Grant No. 2009-0083290) and the Basic Science Research Program (Grant No. 2010-0005366) through the National Research Foundation of Korea (NRF), funded by the Ministry of Education, Science and Technology.

References

1. T. W. Ebbesen, H. J. Lezec, H. F. Ghaemi, T. Thio, and P. A. Wolff, "Extraordinary optical transmission through subwavelength hole arrays," Nature **391**, 667–669 (1998).
2. W. L. Barnes, A. Dereux, and T. W. Ebbesen, "Surface plasmon subwavelength optics," Nature **424**, 824–830 (2003).
3. F. J. Garcia-Vidal, L. Martin-Moreno, T. W. Ebbesen, and L. Kuipers, "Light passing through subwavelength apertures," Rev. Mod. Phys. **82**, 729–787 (2010).
4. D. E. Grupp, H. J. Lezec, T. Thio, and T. W. Ebbesen, "Tunable enhanced light transmission through a single subwavelength aperture," Adv. Mater. **11**, 860–862 (1999).
5. H. J. Lezec, A. Degiron, E. Devaux, R. A. Linke, L. Martin-Moreno, F. J. Garcia-Vidal, and T. W. Ebbesen, "Beaming light from a subwavelength aperture," Science **297**, 820–822 (2002).
6. F. J. Garcia-Vidal, L. Martin-Moreno, H. J. Lezec, and T. W. Ebbesen, "Focusing light with a single subwavelength aperture flanked by surface corrugation," Appl. Phys. Lett. **83**, 4500–4502 (2003).
7. P. T. Worthinga and W. L. Barnes, "Efficient coupling of surface plasmon polaritons to radiation using a bi-grating," Appl. Phys. Lett. **79**, 3035 (2001).
8. H. Kim, J. Park, and B. Lee, "Finite-size nondiffracting beam from a subwavelength metallic hole with concentric dielectric gratings," Appl. Opt. **48**, G68–G72 (2009).
9. S. Seo, H. C. Kim, H. Ko, and M. Cheng, "Subwavelength proximity nanolithography using a plasmonic lens," J. Vac. Sci. Technol. B **25**, 2271–2276 (2007).
10. H. Ko, H. C. Kim, and M. Cheng, "Light transmission through a metallic/dielectric nano-optic lens," J. Vac. Sci. Technol. B **26**, 2188–2191 (2008).
11. D. N. Breslauer, R. N. Maamari, N. A. Switz, W. A. Lam, and D. A. Fletcher, "Mobile phone based clinical microscopy for global health applications," PLoS ONE **4**, e6320 (2009).
12. N. Fang, H. Lee, C. Sun, and X. Zhang, "Sub-diffraction-limited optical imaging with a silver superlens," Science **308**, 534–537 (2005).
13. S. Seo, S. O. Isikman, I. Sencan, O. Mudanyali, T. Su, W. Bishara, A. Erlinger, and A. Ozcan, "High-throughput lens-free blood analysis on a chip," Anal. Chem. **82**, 4621–4627 (2010).
14. X. Luo and T. Ishihara, "Surface plasmon resonant interference nanolithography technique," Appl. Phys. Lett. **84**, 4780–4782 (2004).

15. M. J. Weber, *Handbook of Optical Materials* (CRC, 2003).
16. S. C. Hohng, Y. C. Yoon, D. S. Kim, V. Malyarchuk, R. Muller, Ch. Lienaub, J. W. Park, K. H. Yoo, J. Kim, H. Y. Ryu, and Q. H. Park, “Light emission from the shadows: surface plasmon nano-optics at near and far fields,” Appl. Phys. Lett. **81**, 3239–3241 (2002).
17. G. T. D. Francia, “Super-gain antennas and optical resolving power,” Il Nuovo Cimento **9**, 426–438 (1952).
18. J. L. Harris, “Diffraction and resolving power,” J. Opt. Soc. Am. **54**, 931–933 (1964).
19. A. Ranfagni, D. Mugnai, and R. Ruggeri, “Beyond the diffraction limit: super-resolving pupils,” J. Appl. Phys. **95**, 2217–2222 (2004).
20. H. I. Smith, “A proposal for maskless, zone-plate-array nanolithography,” J. Vac. Sci. Technol. B **14**, 4318–4322 (1996).
21. P. Saari, K. Reivelt, and H. Valtna, “Ultralocalized superluminal light pulses,” Laser Physics **17**, 297–301 (2007).

163.152.230.111 {ts '2022-02-11 01:44:22'}